Surfaces and Interfaces 34 (2022) 102365

Contents lists available at ScienceDirect

Surfaces and Interfaces

journal homepage: www.sciencedirect.com/journal/surfaces-and-interfaces

Tailoring surface properties, biocompatibility and corrosion behavior of stainless steel by laser induced periodic surface treatment towards developing biomimetic stents

Muhammad Saqib [a,d,*], Natalia Beshchasna [a], Riccardo Pelaccia [b], Anton Roshchupkin [c], Ilya Yanko [c], Yevheniia Husak [c,i], Sergiy Kyrylenko [c], Barbara Reggiani [b,e], Gianaurelio Cuniberti [d], Maksym Pogorielov [c,f,g], Joerg Opitz [a,d], Leonardo Orazi [b,h]

[a] Fraunhofer Institute for Ceramic Technologies and Systems IKTS, Maria-Reiche-Strasse 2, Dresden 01109, Germany
[b] Department of Sciences and Methods for Engineering, University of Modena and Reggio Emilia, Via Giovanni Amendola, 2, 42122 Reggio Emilia RE
[c] Biomaterials Research Center, Sumy State University, 31 Sanatorna St, Sumy 40018, Ukraine
[d] Institute of Materials Science and Max Bergmann Center of Biomaterials, Technische Universität Dresden, Dresden 01062, Germany
[e] InterMech MO.RE., Tecnopolo di Reggio Emilia, 1 Piazzale Europa, Reggio Emilia 42124, Italy
[f] Institute of Atomic Physics and Spectroscopy, University of Latvia, 3 Jelgavas iela, Riga LV-1004, Latvia
[g] NanoPrime, 25 Metalowcow St, Dedice 39-200, Poland
[h] En&Tech, Tecnopolo di Reggio Emilia, 1 Piazzale Europa, Reggio Emilia 42124, Italy
[i] Faculty of Chemistry, Silesian University of Technology, Gliwice 44-100, Poland

ARTICLE INFO

Keywords:
Nanopatterns
Picosecond laser
Surface roughness
Surface free energy
Corrosion
Umbilical cord mesenchymal stem cells
Biocompatibility
Cell orientation

ABSTRACT

Laser-Induced Periodic Surface Structures (LIPSS) holds great potential for regenerative biomedicine. Creating highly precise LIPSS enables to generate biomimetic implant surfaces with improved properties. The present study focuses on the fabrication and investigation of laser-treated stainless steel samples with applied linear LIPSS patterns with grooves made by means of a picosecond laser system using wavelengths of 1064 nm and 532 nm. To investigate properties of the laser-treated surfaces and to understand the basics of cell-surface interactions between the LIPSS and human Umbilical Cord Mesenchymal Stem Cells (UCMSC), flat stainless steel samples with various applied nanopatterns were used. Such LIPSSs demonstrated higher surface roughness, good biocompatibility, lower wettability and higher corrosion resistance compared to the untreated (polished) specimens. The surface roughness of laser-treated samples was in microscale that enabled adhesion and migration of endothelial cells, thus increasing the likelihood for endothelialisation. This thereby could reduce the chances for the development of Late Stent Thrombosis (LST) and In-Stent Restenosis (ISR). Furthermore, laser textured surfaces demonstrated an environment supportive for cell attachment, proliferation and alignment with the nanogroves. Therefore, application of the biomimetic nanopatterns could help to overcome frequent post-surgery complications after the stent implantation.

1. Introduction

Coronary artery disease (CAD) causes angina pectoris, ischemic heart failures, myocardial infarction (MI) and many other related pathologies. Together, they become the top cause of mortality all over the world [1]. CAD is initiated by the formation of atherosclerotic plaques on the inner walls of blood vessels, leading to lumen obstruction. Four decades ago percutaneous coronary intervention (PCI) was introduced as a first-line method in treatment of the acute CAD [2] that reduced MI subsequent and deaths [3]. The first stainless steel, self-expanding mesh stent (bare-metal stents, BMS) was implanted in 1986 [4] and turned out to be a clinical success. However, retrospective studies demonstrated high risk of in-stent restenosis (around 20–30%) in the period of 6–9 month after the stent placement [5,6]. Different variations of BMS design, materials, and coatings were attempted with little clinical effects on restenosis rate even with the support of dual antiplatelet therapy [7]. Based on different clinical trials, Drug-Eluting Stents (DES) were used for infusion of antiproliferative drugs with direct action on the endothelium of the

* Corresponding author at: Fraunhofer Institute for Ceramic Technologies and Systems IKTS, Maria-Reiche-Strasse 2, Dresden 01109, Germany.
E-mail address: muhammad.saqib@ikts.fraunhofer.de (M. Saqib).

https://doi.org/10.1016/j.surfin.2022.102365
Received 23 June 2022; Received in revised form 7 September 2022; Accepted 19 September 2022
Available online 21 September 2022

coronary artery to prevent restenosis [8]. Two generations of DES became available in medical market since 2003 based on the BMS platforms with antiproliferative drugs in polymeric drug depot which allowed a controllable release. First generation DES contained paclitaxel or sirolimus as the antiproliferative agents [9], while second generation DES employed lipophilic agents everolimus or zotarolimus; and used chromium based frames [10]. Both generations of the DES demonstrated superiority in early in-stent restenosis and target vessel revascularization compared to the BMS [11]. However, the release of the antiproliferative compounds diminished within 6–9 months [12], leading to frequent late stent thrombosis after DES placement [13]. Taking this into account, variuos modifications of metal stents have been proposed to prolong antiproliferative effect and to allow for the appropriate endothelization. These included electrochemical cyclic potentiodynamic passivation [14], pulsed-plasma polymeric allylamine films [15], titanium oxynitride (TiO_xN_y) coatings via magnetron sputtering [16,17], ion implantation and deposition [18] to mention a few.

On the other hand, nanopatterning on the implant surfaces could affect endothelialization, cell proliferation, platelet adhesion and cell alignment [19]. Therefore, by controlling geometry and dimension of the nanostructures, the clinical outcome of stent technology can ultimately be improved.

Laser-induced periodic surface structuring has recently emerged as one of the promising surface modification techniques to avoid LST and ISR. LIPSSs are an arrangement of (quasi) periodic topographic lines representing a linear surface grating structure [20]. LIPSS has already been successfully used for applications in optics [21], electronics [21], fluidics [22], mechanical engineering [23,24] and medicine [25]. LIPSS are generated by irradiating the surface with short and ultra-short laser pulses with a fluence slightly above the ablation threshold. This generates quasi-ordered nanostructures with periodicities in the order of the utilized laser wavelength and orientation driven by beam polarization [26]. LIPSS can be fabricated on almost all types of materials, including metals, semiconductors and dielectrics following a single-step, direct--writing technique as a flexible, robust, rapid and contactless process [26]. Depending on their shapes, LIPSS structures can be named ripples, nanoripples, fibrils, reliefs, micrometric grooves or spikes, with characteristic dimensions of the same order of about one order of magnitude lower than the laser wavelength [20].

Although LIPSS technique offers a fast-processing treatment, it is still complicated to get ultimate control on the LIPSS processing, to preserve the surface functionality in the long term, and to make use of it on the complex geometrical surfaces e.g. stents.

Reproducible fabrication of highly regular LIPSS to create biomimetic structures on metallic materials such as nickel (Ni), aluminum (Al) and its alloys, copper (Cu), molybdenum (Mo), titanium (Ti) and its alloys, magnesium (Mg) and its alloys and stainless steel for medical applications, in particular for implantable materials, has been summarized in [27]. The fabrication of these biomimetic surfaces was aimed at creating surfaces more hydrophilic/hydrophobic, corrosion-resistant, wear-resistant, mechanical fatigue resistant, bactericidal, etc. The ongoing research in the field of LIPSS suggested the significance of chemical effects accompanying the LIPSS formation and the long-term stabilization of the surface wetting characteristics (e.g., hydrophobicity or hydrophilicity) will represent one of the main future trends of research on LIPSS for biomedical applications [25].

Many studies reported that laser treatment on metal surfaces improved the corrosion behavior of the metals [28–34]. For instance, the Ti-6Al-4 V alloy treated with excimer laser showed a strong increase in corrosion resistance [29]. Moreover, the corrosion resistance of laser patterned aluminum surfaces was improved by about 11 folds as compared to untreated aluminum [33]. The nanopatterns on calcium phosphate coated Ti–6Al–4 V with power densities between 25 and 50 W/mm^2 via Nd:YAG (neodymium-doped yttrium aluminum garnet; Nd:$Y_3Al_5O_{12}$) laser also reported the improved corrosion and mechanical behavior in simulated body condition [30]. Similarly, Geetha et al. 2004 [31] modified the β-alloy Ti-13Nb-13Zr surface using a Nd:YAG laser under nitrogen atmosphere, reporting a significant increase of corrosion resistance of laser nitrided samples compared to untreated ones in simulated body condition. More recently, the superior corrosion of SS316L surface with nanotextures with the inhibition of pathogenic Gram-positive and Gram-negative bacteria has been reported [32]. The mechanism behind this superior corrosion resistance was the entrapment of air bubbles in the grooves. This could prevent the contact of corrosive species (such as Cl^-) with the sample surface. In summary, the main reasons for the corrosion improvement were the microstructural changes [29] in the base material and the specific surface patterns that caused air bubbles to trap in the cavities [33] reducing the solid-liquid contact area [34] thus improving the corrosion behavior.

Biomimetic coatings (such that peptide coating, endothelium-like coating, etc.) improved the biocompatibility and corrosion resistance of implants [35–37]. Similarly, biomimetic patterns on implant surfaces applied using laser irradiation were also aimed to improve the endothelialization, cell proliferation and alignment with the enhanced mechanical and corrosion behavior as a result [27,38,39]. For example, the vascular smooth muscle cells (VSMCs)-biomimetic surface pattern with nanofibers at 0.7 μm diameter on 316 L surface was shown to promote attachment, proliferation and migration of HUVEC (human umbilical vein endothelial) cells in cultures in vitro [39]. Furthermore, the rapid re-endothelialization was significantly improved using these biomimetic surfaces as compared with control samples for 30 and 90 post-implantation days. The effect of various nanopatterns on cellular adhesion, proliferation and alignment was well described in the latest review by Dong et al. 2022 [19]. In general, variable textures on the surface can allow to control cell adhesion, proliferation and alignment.

Based on vast potential of LIPSSs to improve various properties of the implants, including their biocompatibility, surface properties, and resistance agains corrosion, the current project was focused on the development of biomimetic structures on 316 L steel samples to enable biomimetic platform to manufacture cardiovascular stents. We produced 3 different laser structured surfaces i.e., 1) linear LIPSS (reliefs) with 1064 nm, 2) linear LIPSS with 532 nm LIPSS, and 3) Grooves with 532 nm. The samples presented in this work were used to perform two different surface evaluations i.e., (a) linear LIPSS v/s grooves, and (b) linear LIPSS with 532 nm v/s 1064 nm. The biocompatibility was assessed using human umbilical cord mesenchymal stem cells. The electrochemical corrosion behavior was investigated in the Hanks' Balanced Salt Solution (HBSS). The morphology and structure of the surfaces were evaluated by the scanning electron microscopy with energy dispersive X-ray analysis (SEM-EDX), contact angle, laser profilometry, electrochemical corrosion assay, etc. In general, the LIPSS samples have shown significantly improved corrosion behavior and biocompatibility as compared to the untreated control samples. As such, this project forms the basis of the development of biomimetic and personalized stents.

However, the industrial implementation of LIPSS technology still needs fundamental understanding of the technological parameters such as minimum structural size, regular quantification and control of the LIPSS geometry and visualization, as well as reproducible fabrication. Some of these issues have been described in [40] while examples of ultrafast laser treatment of complex geometries can be found in [27].

2. Materials and methods

AISI 316 stainless steel samples were obtained from a plate 2 mm in thickness by laser cutting disks 10 mm in diameter. Samples were then polished by means of the universal polisher *Remet LS 2 A* using sample holders fabricated by additive manufacturing showed in. This step permitted to prepare more specimens simultaneously. The samples were firstly grinded with silicone carbide abrasive papers, using the standard grit sequence 240/400/800/1000/2500. The samples were washed with 98% ethanol after each grinding step to remove the residual debris of the

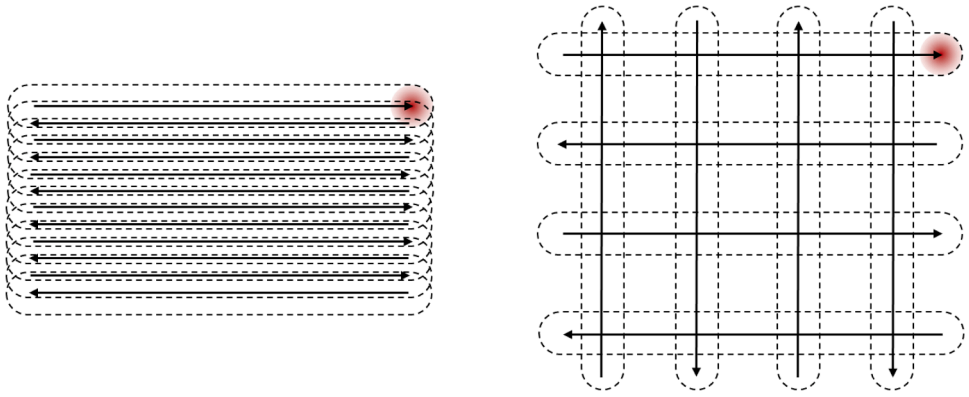

Fig. 1. Left) patterning strategies relative to L_{1064} and L_{532} conditions. Right) patterning strategies relative to L_{Gv} condition.

previous step. Afterwards, two polishing cloths were selected for the final mirror polishing using diamond polishing suspensions with grain size of 6 μm and 1 μm.

2.1. Sample preparation using laser induced periodic surface treatment

Laser treatments were performed using EKSPLA Atlantic 5 pico-second laser. The laser emits pulses 10 ps in length and integrates a higher harmonics generator. In this work beamlines with wavelength of 1064 and 532 nm were employed. Samples were patterned using two Raylase Superscan V scanning heads with an input aperture of 14 mm and equipped with 80 mm focal length F-theta lenses. Beam expanders are inserted in the beamlines to take advantage of the relatively high numerical aperture and, taking in considerations the beam quality of the laser ($M^2 = 1.3$) the scanners can focalize the laser beam on a $1/e^2$ diameter of 12 and 10 μm for, respectively, the first and second harmonics.

Three different scanning conditions were investigated, two of them, L_{1064} and L_{532}, aimed to obtain on the surfaces a uniform distribution of LIPSS, while the third, L_{Gv}, was to generate a grid of grooves 40 μm in spacing. These conditions were moreover compared with the untreated polished samples L_0. The kinematic aspects of the patterning conditions are described in Fig. 1.

Table 1 summarizes the parameters of the laser treatments. The procedures to obtain LIPSS were performed with first and second harmonics, the combination of scanning speed, pulse repetition rate and hatch space generated a uniform distribution of pulses, equally overlapped along and between scanlines while multiple crosshatch passes using the 532 nm beamline with a sidestep of 40 μm were used for the direct laser writing of grids. Laser parameters are indicated both in terms of laser source parameters and with more meaningful physical parameters like fluence (related to the single pulse) and dose corresponding to the fluence accumulated by pulse overlapping and passes.

The kinematics aspects of the patterning strategies are summarized in Fig. 1.

2.2. Characterization methods (SEM, contact angle (CA), surface free energy, laser profilometry)

2.2.1. SEM

All the SEM images for electrochemical tests were taken using the Environmental Scanning Electron Microscope XL30 ESEM FEG (Philips, Netherlands), or otherwise as specified. The accelerating voltage was set to 3.0 kV with spot size of 3 nm. For all samples, SEM images before and after the corrosion tests were taken. The corroded samples were first cleaned in acetone, ethanol, and ultrapure water, respectively in an ultrasonic water bath for 3–5 min in each liquid.

2.3. Contact angle measurements

CAs were measured using standard optical contact angle measuring and contour analysis systems Dataphysics OCA20. Static water CAs were measured by using 1 μl droplets of distilled water using 0.52 mm diameter syringe. The CAs are presented as the average of at least five readings per sample.

2.4. Surface free energy calculation

The surface free energies of LIPSS and control samples were calculated using Owens, Wendt, Rabel, and Kaelble (OWRK) method (Owens Wendt 1969). To use this method, contact angle measurements with at least two liquids are needed. In this study, three standard test fluids were used i.e. formamide, dimethyl sulfoxide (DMSO), and water. Contact angles with all these fluids were measured at least five times for estimation of the surface energies.

2.5. Owens–Wendt method

The Owens–Wendt or OWRK method is also called the extended Fowkes method. This method combines the two fundamental equations that describe the interactions between solids and liquids. The two equations are Young's (1) and Good's (2) equations [41,42].

Table 1
Laser parameters for surface treatments.

	Wavelength(nm)	Power (W)	Repetition rate [f] (kHz)	Vs (mm/s)	Hatch space (μm)	# Passes	Pulse fluence (J/cm^2)	Dose (J/cm^2)
L_0	–	–	–	–	–	–	–	–
L_{1064}	1064	0.5	300	1200	4	1	1.5	13.3
L_{532}	532	0.12	300	1200	4	1	0.5	3.2
L_{Gv}	532	1.2	100	1500	40	60	14	560

Table 2
The components of the surface energy of test liquids were obtained from [43, 44].

Test liquid	γ_l (mN/m)	γ_l^p(mN/m)	γ_l^d (mN/m)
Water	72.8	51	21.8
DMSO	44	8	36
Formamide	58	19	39

Note: γ_l, the overall surface energy of liquid; γ_l^p, the polar component surface energy of liquid; γ_l^d, the dispersive component surface energy of the liquid.

$$\gamma_{sv} - \gamma_{sl} = \gamma_{lv}\cos\theta \tag{1}$$

where θ is the contact angle, and γ_{sv}, γ_{sl}, γ_{lv} refers to the interfacial tension (γ) between the solid-vapor (*sv*), solid-liquid (*sl*), and liquid-vapor (*lv*) interfaces, respectively.

$$\gamma_{sl} = \gamma_s + \gamma_l - 2\left(\gamma_s^d\gamma_l^d\right)^{1/2} - 2\left(\gamma_s^p\gamma_l^p\right)^{1/2} \tag{2}$$

where γ_s, γ_l are the surface tension in the solid and liquid; γ_s^d, γ_l^d are the dispersive surface tension components, whereas γ_s^p, γ_l^p are the polar surface tension components for solid and liquid, respectively.

$$\frac{\gamma_l(\cos\theta+1)}{2\left(\gamma_l^d\right)^{1/2}} = \left(\gamma_s^p\right)^{1/2}\frac{\left(\gamma_l^p\right)^{1/2}}{\left(\gamma_l^d\right)^{1/2}} + \left(\gamma_s^d\right)^{1/2} \tag{3}$$

As we know that linear equation of a line with slope and intercept is,

$$y = mx + b \tag{4}$$

Comparing Eqs. (2) and 3 we get,

$$x = \frac{\left(\gamma_l^p\right)^{1/2}}{\left(\gamma_l^d\right)^{1/2}}, \tag{5}$$

$$y = \frac{\gamma_l(\cos\theta+1)}{2\left(\gamma_l^d\right)^{1/2}}, \tag{6}$$

$$m = \left(\gamma_s^p\right)^{1/2}, \tag{7}$$

$$and\ b = \left(\gamma_s^d\right)^{1/2} \tag{8}$$

The polar and dispersive components are known (Table 2). Therefore, by plotting the X against Y and with linear regression we can get the polar and dispersive components of the surface energy as the square of the *m* and the *b*, respectively.

According to this method, the total surface energy is the summation of the polar and dispersive components of the surface energy.

$$\gamma_s = \gamma_s^p + \gamma_s^d \tag{9}$$

2.6. Surface roughness analysis

For the surface roughness analysis, the SurfCharJ 1q plugin of Image J (NIH, USA) used as described previously in other works [45,46]. This plugin measures roughness parameters according to the ISO 4287/2000. SEM images of magnification 40k were used for L_o, L_{1064}, and L_{532}, whereas 1k magnification was used to for L_{Gv} because of its different surface structure. The 3D surface plots of all samples were also obtained using the Image J (NIH, USA).

2.7. Electrochemical cell

The electrochemical cell modified from [16] was used. 316 L LIPSS surfaces were placed as the Working Electrode (WE). Saturated Calomel Electrode [Hg_2Cl_2 (SCE)] KE10 (Sensortechnik Meinsberg, Germany) was used as a Reference Electrode (RE) and a platinum rod (3 mm diameter) was used as a Counter Electrode (CE). The electrochemical cell was electrically coupled to Autolab PGSTAT204 (Metrohm, Switzerland) and the data recording was performed by Nova advanced electrochemical Software 2.x (Metrohm, Switzerland).

2.8. Electrochemical corrosion assay

All electrochemical investigations were performed at room temperature of about 25 °C. Each sample was immersed in 50 ml HBSS with an exposed metallic surface area of 28.27 mm^2. Before any potentiodynamic measurement, the open-circuit potential (OCP) was recorded after 30 min potential-stabilizing immersion period of the working electrode in the HBSS.

Following the OCP measurement, the current density (i [mA/cm^2]) was recorded as a function of the WE potential (E [V] vs. SCE). Potentiodynamic polarization was varied from −1.0 to +1.0 V for all samples with a scan rate of 10 mV/s for each measurement. The step size between two points was set to 1 mV. The Tafel curves were obtained by plotting the logarithmic values of the current density as a function of WE potential (E [V] vs. SCE). The obtained Tafel curves were extrapolated in the Nova advanced electrochemical Software 2.x (Metrohm, Switzerland) to get the corrosion current density (i_{corr}) and the corrosion potential (E_{corr}). The measurement data was then transferred to Origin 2022 (Origin Lab Corporation, Northampton, MA, USA) and the Tafel curves were reproduced. The corrosion rates of LIPSS surfaces were calculated using the following formula:

$$CR = K_1\frac{i_{corr}}{\rho}\ EW \tag{10}$$

where CR is the corrosion rate (mm/yr), K_1 is the constant and its value is 3.27×10^{-3} (mm g/μA), i_{corr} is the corrosion current density (μA/cm^2), ρ is the standard density (g/cm^3), and EW is the equivalent weight (g/eq).

2.9. Assessment of biocompatibility in cell cultures in vitro

The culture of mesenchymal stem cells obtained from human umbilical cord was maintained using standard methods of cell cultures at 37 °C in the atmosphere with 5% CO_2. Fresh medium was added every 2 or 3 days. Standard DMEM/F-12 medium with 10% FBS (fetal bovine serum) was used with L-glutamine in the presence of 100 units/ml penicillin, 100 μg/ml streptomycin and 0.25 μg/ml amphotericin B. The samples after hot-air sterilization were incubated in 24-well cell culture plates with the complete growth medium overnight. The next day the UCMSCs were plated into the wells with the LIPSS samples, as well as into sample-free wells (as positive control), at 10 000 cells/cm^2 in 1 ml of the culture medium. Cell-free medium was used as negative controls. Resazurin reduction assay was used to evaluate cellular adhesion and proliferation after 1, 2 and 3 days post-plating. The plates with resazurin at 15 μg/ml were incubated at 37 °C in the cell culture incubator for 8 h. One hundred μl aliquots of medium with resazurin were taken and placed into fresh 96-well plates for measurement of optical densities at 570 nm and 595 nm in Multiskan FC (Thermo Fisher Scientific, Waltham, MA, USA) equipment. The results were analyzed as previously described [47].

For fluorescence microscopy, the discs were quickly rinced in 1 ml PBS and stained with DAPI (4′,6-diamidine-2′ -phenylindole dihydrochloride, Roche) in PBS. The samples were analyzed with the Axio Imager A1 microscope (Carl Zeiss, Yena, Gemany).

2.10. Characterization of the LIPSS after cell culture experiment

The samples were fixed in neutral 4% formaldehyde for 10 min, rinsed in PBS, dehydrated in the increasing concentrations of ethanol and air dried. The surface morphology of the discs with cells was

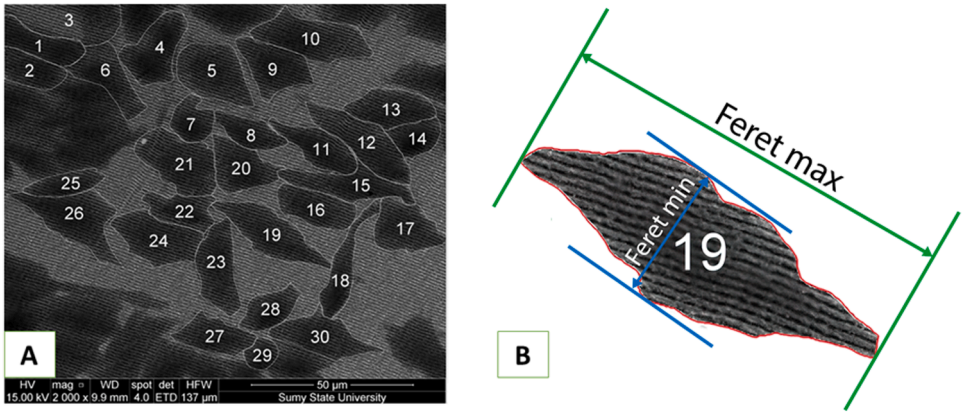

Fig. 2. A drawing which shows processing of cell borders by the ImageJ software (A) and the scheme to explain measurement of Feret diameter where a cell #19 from the panel A was taken as an example (B).

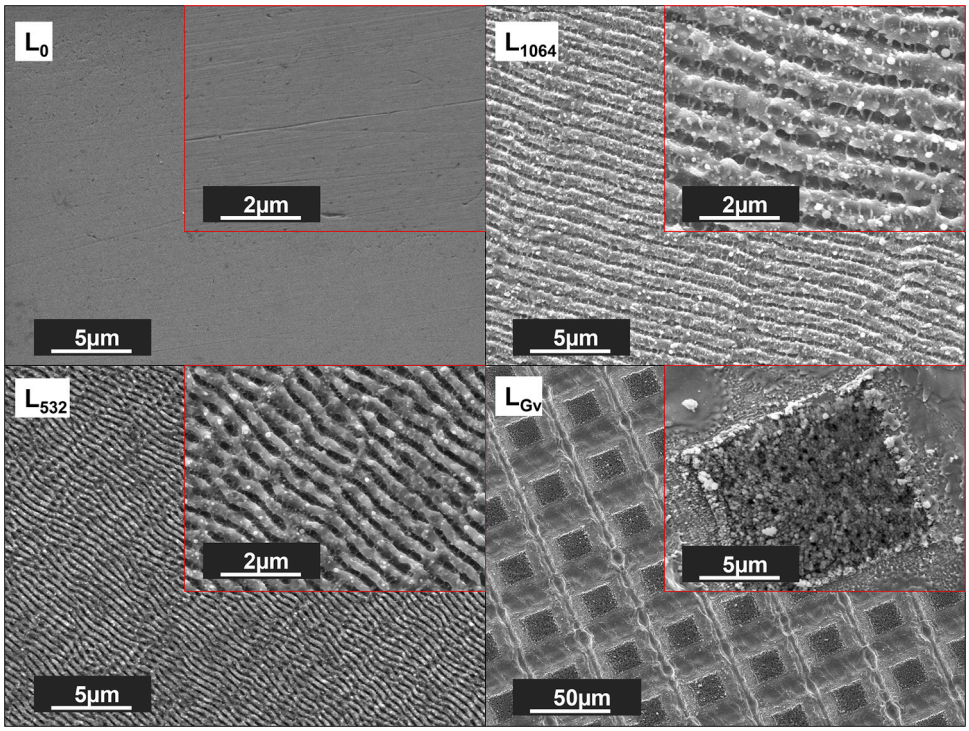

Fig. 3. Surface morphology of the control and irradiated samples before the electrochemical corrosion test.

accessed with scanning electron microscope Inspect S50B (FEI, Brno, Czech Republic) at 25 kV acceleration voltage.

2.11. Cell shape and orientation

SEM images were analyzed using ImageJ software to access geometric properties of the cells. Only the cells with clear cut borders were taken for analysis. Minimum and maximum Feret diameter, as well as Feret angle in relation to the direction of the LIPSS pattern were measured. The aspect ratio was calculated as ratio of maximum and minimum Feret diameters (Fig. 2).

Statistical analysis was done by Graphpad Prism v.9.2.0 software. First, the Normality test from the "Normality and lognormality" section was performed on aspect ratio values. Statistical difference was accessed with the two-tailed non-parametric *t*-test. A frequency distribution test with 20° steps was performed for the Feret angles (angle between maximum Feret diameter of the cells and the X axis), and the data was presented at a graph with indications of the angle between the LIPSS pattern and the X axis. The average angles between the LIPSS patterns on the sample and the X-axis of the image were also measured and shown on the graph as color coded vertical lines.

3. Results and discussion

3.1. Surface morphology (SEM & laser profilometry)

Fig. 3 shows the surface topography of all the samples before experiments. It verifies that the regular LIPSS patterns and the grooves with 40 µm spacing were achieved. The small white crystal on the LIPSS reliefs is the solidified form of steel that was melted during the laser irradiation. The average width of the LIPSS reliefs calculated by image J for L_{1064} and L_{532} is 0.58 (±0.04) µm and 0.22 (±0.02) µm, respectively. Similarly, the gap between two adjacent reliefs for, respectively, L_{1064} and L_{532} is 0.37 (±0.05) µm and 0.21 (±0.02) µm. However, the square structures in the L_{Gv} are 20 µm × 20 µm with the 40 µm spacing from their centers. The squares are also more granular than the linear LIPSS reliefs.

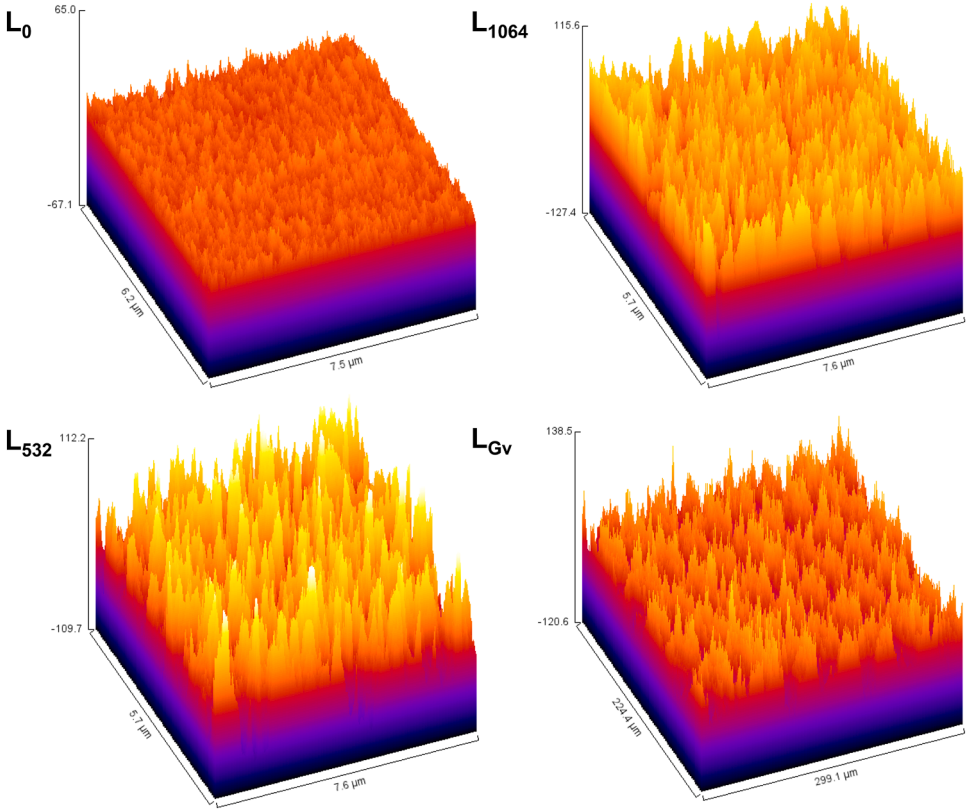

Fig. 4. 3D Surface plots obtained by Image J (NIH, USA).

Fig. 4 shows the 3D images of the L_0 and L_{Gv}, respectively. The surface roughness parameters R_t (maximum height of the profile), R_a (average roughness) and R_q (root mean square deviation of the profile) are presented in Table 3. All irradiated surfaces show increased average roughness as compared to the polished 316 L surface. The average roughness of L_{532} is 0.19 µm, the lowest in laser-irradiated samples, whereas the L_0 has the average roughness of 0.05 µm, the lowest among all samples tested. L_{Gv} showed the highest average roughness of 10.4 µm which is 51 folds more than L_{1064} and 55 folds more than the L_{532}. The root mean square deviation of the profile in L_0, L_{1064}, L_{532}, and L_{Gv} is 0.06 µm, 0.25 µm, 0.22 µm, and 16.64 µm, respectively. The R_q of L_{Gv} is nearly 67 folds that of L_{1064} and 74 folds that of L_{532}. Moreover, the maximum height of the profile in L_0, L_{1064}, L_{532}, and L_{Gv} is 0.65 µm, 1.13 µm, 1.15 µm, and 55.81 µm, respectively. The big difference in the R_t for L_0 from R_a is due to the damaged or scratched parts in the scanning. Concisely, all irradiated samples display the increased surface roughness which in turn decreases the rate of corrosion or increases the corrosion resistance [34].

3.2. Wettability and surface free energy

Fig. 5 shows the static water CAs for all surfaces before the corrosion biocompatibility test. The CAs for all LIPSS surfaces were in the range of 113° to 114°, where L_{1064} has the highest CA i.e., 114° However, the polished 316 L sample (L_0) has CA of 87° These CAs show that all the LIPSS samples become hydrophobic after the laser treatment, as the polished 316 L was hydrophilic.

It is well known that low contact angles lead to good adhesiveness and wettability, whereas the high contact angles correspond to poor adhesiveness and wettability [48]. Therefore, it can be interpreted that the LIPSS treatment turned the wettability low and reduced the interaction between the solid-liquid phase which increased the interaction between the liquid-liquid phase. The lowest wettability was obtained by the L_{1064} surface.

Table 4 shows the CAs of all samples in three different test fluids,

Table 3
Surface roughness parameters (in µm): R_a, R_q, and R_t analyzed by SurfCharJ plugin (ImageJ, NIH, USA).

Roughness parameters	L_0	L_{1064}	L_{532}	L_{Gv}
R_a	0.05	0.20	0.19	10.42
R_q	0.06	0.25	0.22	16.64
R_t	0.65	1.13	1.15	55.81

Note: R_a is average roughness, R_q is the root mean square deviation of the profile, and R_t is the maximum height of the profile.

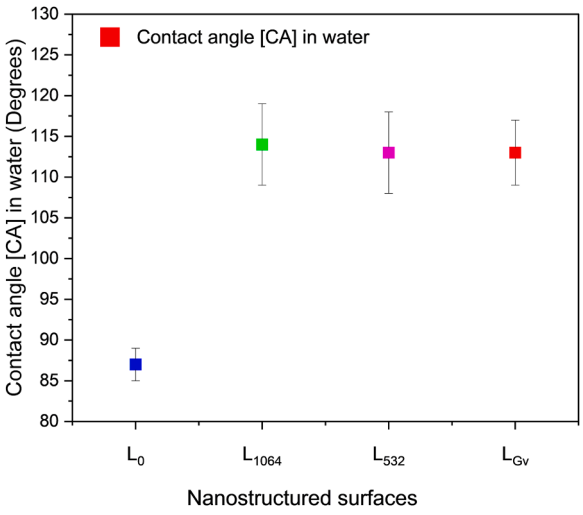

Fig. 5. Static water contact angles of the surfaces.

Table 4
Contact angles of all surfaces in three different fluids.

Sample	Water	DMSO	Formamide
L_0	87 (± 2)	52 (± 2)	80 (± 2)
L_{1064}	114 (±5)	52 (±3)	83 (±4)
L_{532}	113 (±5)	50 (±8)	82 (±2)
L_{Gv}	113 (±4)	37 (±2)	82 (±3)

Table 5
Surface energy and its components.

Sample	Υ_l (mN/m)	Υ_l^p (mN/m)	Υ_l^d (mN/m)
L_0	82.7 (± 1.3)	80.2 (± 0.9)	2.5 (± 0.9)
L_{1064}	78.0 (±1.0)	77.4 (±0.7)	0.6 (±0.7)
L_{532}	74.6 (±0.1)	62.4 (±0.1)	12.2 (±0.1)
L_{Gv}	78.1 (±0.9)	70.2 (±0.6)	8.0 (±0.6)

namely water, DMSO, and formamide. Unlike static water contact angles for all samples, the CAs of LIPSS surfaces and the control sample are nearly the same. The only significant difference was found in the CA of L_{Gv} sample as compared to other LIPSS surfaces and the polished sample. The possible reason for such a small CA of Groove surface in DMSO could be its large step size of 40 μm combined with the low viscosity of the DMSO (1.991 mPas) as compared to the formamide (3.302 mPas), while the CAs of all surfaces are nearly the same and in the range of 80°−83° Furthermore, the CAs in DMSO are smaller for all samples as compared to the CAs in formamide, which is in agreement with the results presented by Zhang et al. 2019 [44]. Additionally, the low surface tension of DMSO is the main reason of low contact angles [49].

Fig. 6 shows the data points obtained by using Eqs. (3) and (4) with their linear fitting to obtain the polar and dispersive surface energy components for the calculation of total surface energies by the Owens–Wendt method. Table 5 shows the total surface energy and its components (polar and dispersive) for all samples obtained with the linear fitting.

The untreated polished sample L_0 showed the highest surface energy among all samples which is in agreement with the existing literature. The lowest surface energy was obtained by the L_{532} sample, whereas, L_{Gv} had the highest surface energy among treated samples. Surface energy of the solid is the product of surface tension of the liquid and the exposed area of solid surface, therefore, due to the variation in exposed surface area as a result of the laser patterning, the surface energy is changed for all laser textured samples. Surprisingly, L_{1064} and L_{Gv} showed similar total surface free energies, but their polar and dynamic surface energy components are different. This is because of the different microstructure on the surface of the samples, exposed area, and surface topography with the 1064 nm and 532 nm laser treatment that enforced this difference. The laser treatment caused hydrophobicity and lower surface energies in all treated samples as compared to the L_0. The order of

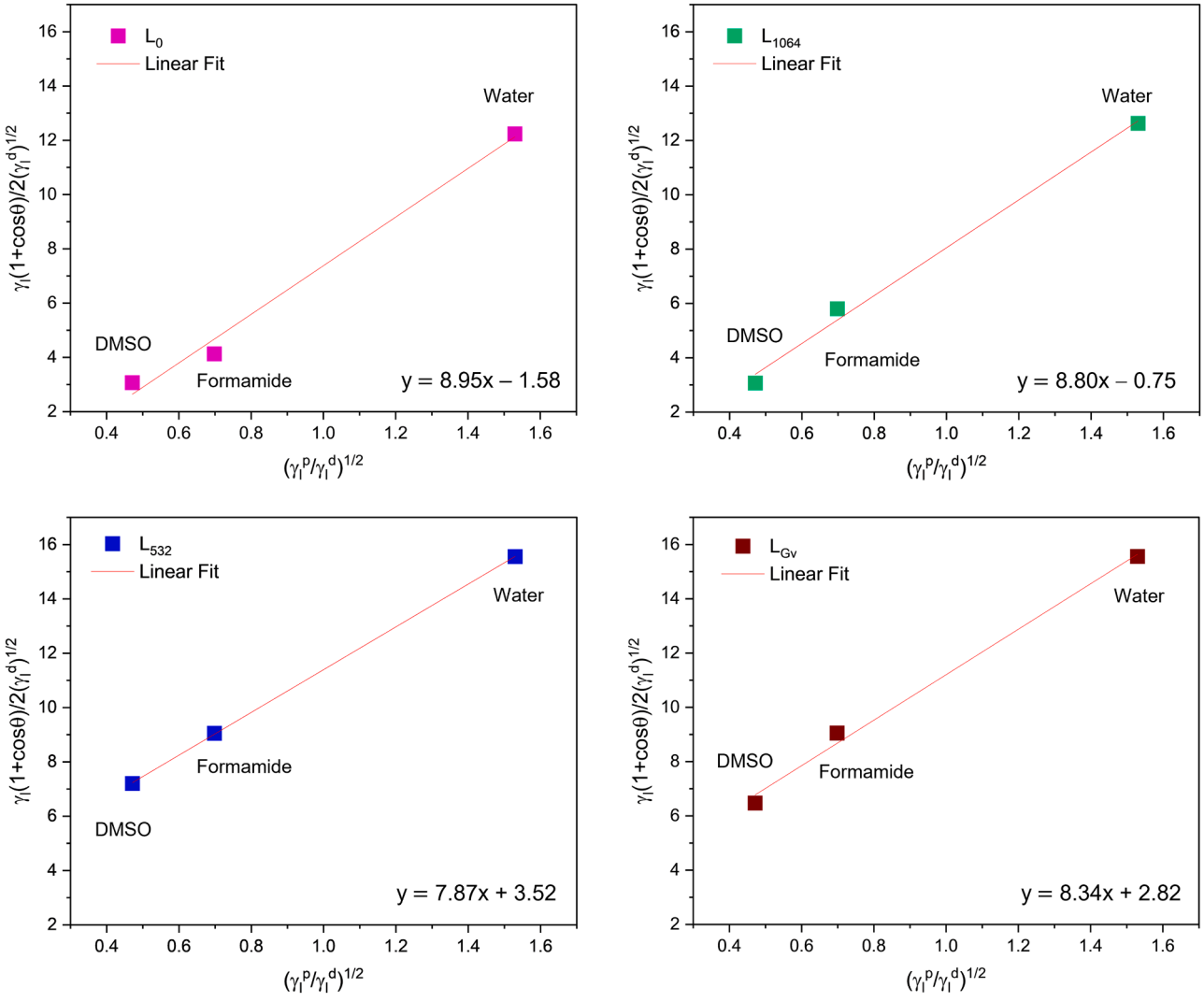

Fig. 6. Linear fitting by OWRK method.

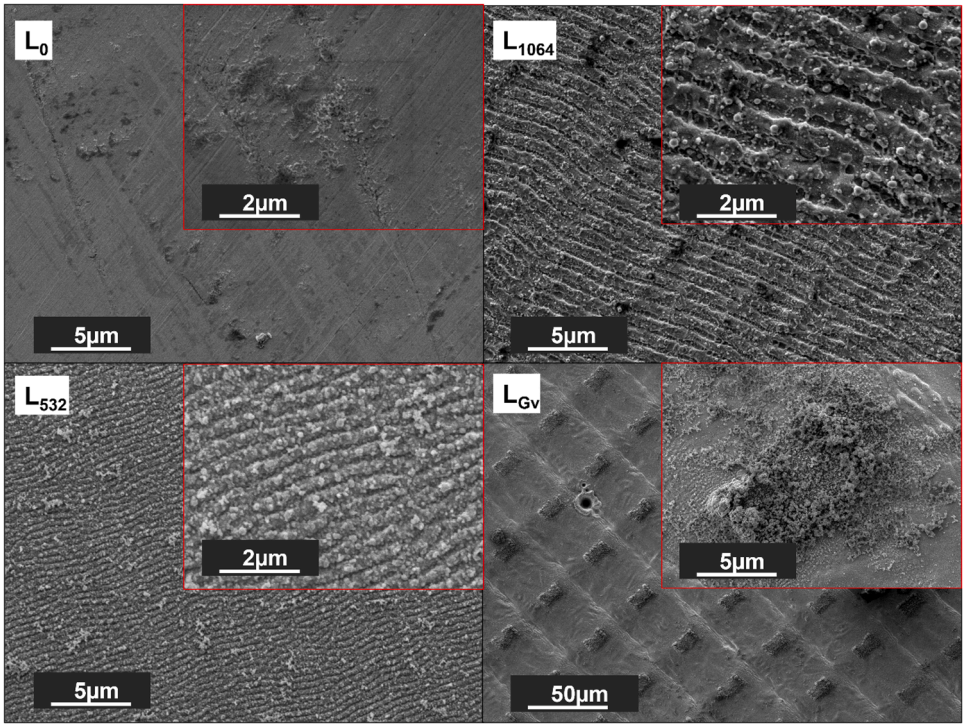

Fig. 7. Surface morphology of control and irradiated samples after electrochemical corrosion test.

increasing surface energies in laser patterned samples is $L_{532} < L_{1064} < L_{Gv} < L_0$.

3.3. Surface morphology after electrochemical exposure

Fig. 7 indicates the surface morphology of all samples with clear signs of degradation after the electrochemical attack. The surface of L_0 lost its smoothness and the corrosion products can be seen on its surface. In the case of L_{1064} and L_{532}, the height of LIPSS structures was reduced due to material loss. The L_{532} surface became more granular than the L_{1064}, the width of the LIPSS reliefs was increased and thus reducing the spacing between reliefs. The phenomenon was not prominently observed in the L_{1064}. There were some pits observed in both aforementioned samples with the random diameter. In the case of L_{Gv}, the rectangular patterns between grooves become smaller in size and thus increasing the groove spacing. Due to the five sides of this structure facing the HBSS, these structures were severely attacked in the electrochemical experiment. The lost material, as the corrosion product spread around these structures.

Fig. 8a and 8b show two different pits that were observed in the L_{1064} sample. Interestingly, the LIPSS structures behaved like a coating, where this coating was there even when the material beneath this coating was removed. Furthermore, these delaminated LIPSS structures can be seen on the pits as perpendicular to the LIPSS plane (Fig. 8a) and parallel to

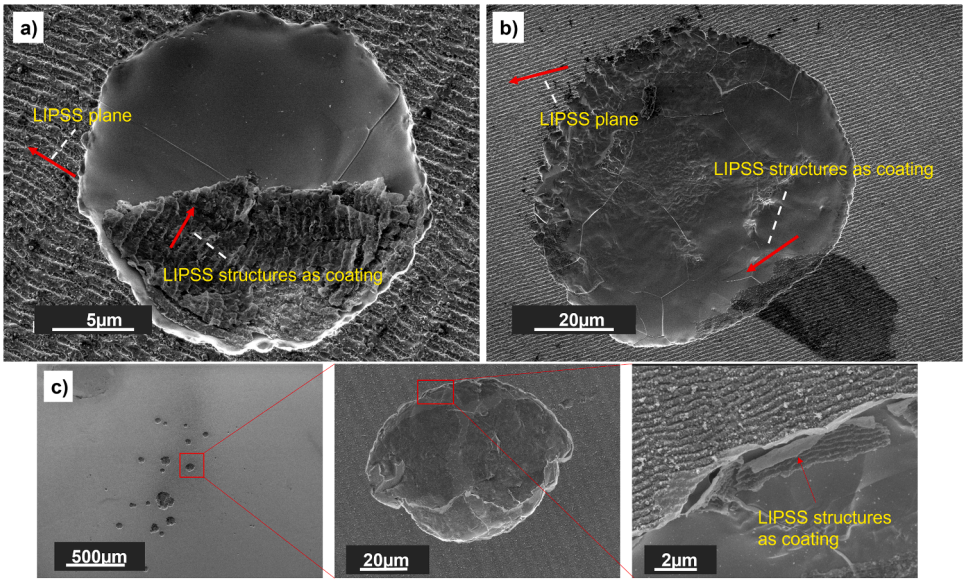

Fig. 8. LIPSS structures as a coating: (a) perpendicular to the LIPSS plane (Magnification:10 K) in L_{1064}, and (b) parallel to the LIPSS plane (Magnification:20 K) in L_{1064}, and (c) pits formation and LIPSS structures as a coating (Magnification: 250, 10 K, and 20 K) in L_{532}. The red arrows show the LIPSS plane.

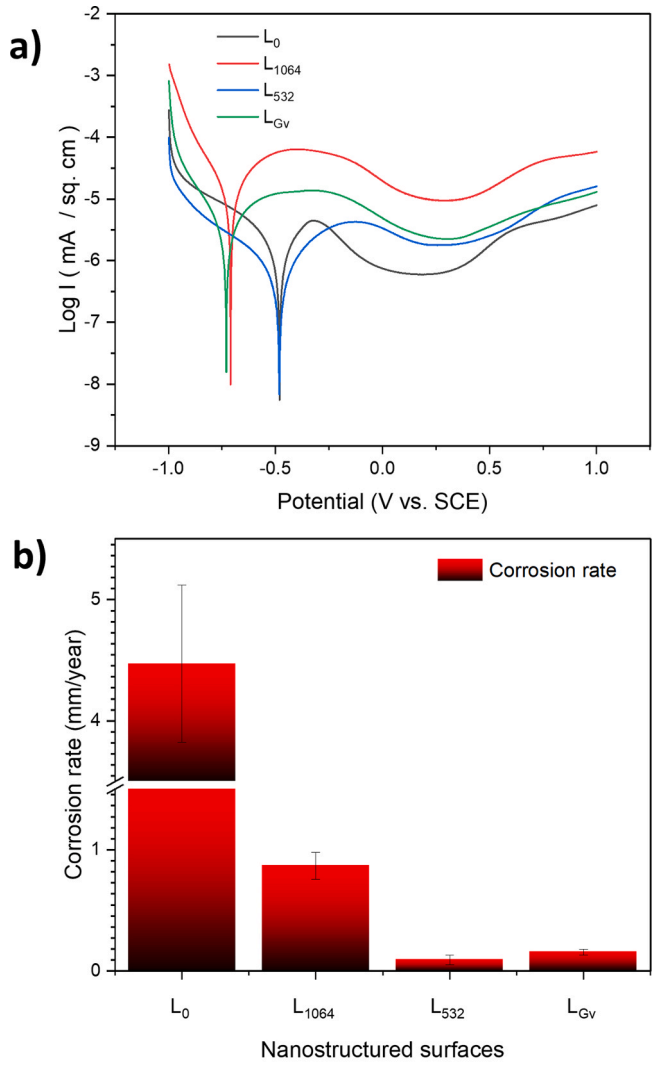

c)

LIPSS Surface	Increase in corrosion resistance / decrease in corrosion rates [X times]
L_0	1
L_{1064}	5.5
L_{532}	48.8
L_{Gv}	28.5

Fig. 9. Corrosion behavior of LIPSS surfaces: (a) Tafel curves, (b) Bar chart for corrosion rates, and (c) The ratio of increase in corrosion resistance after laser irradiation.

the LIPSS plane (Fig. 8b). This result suggests the presence of strong intermolecular forces between the molecules on the surface because of laser treatment.

A similar kind of behavior can be seen of LIPSS structures in the case of L_{532} (Fig. 8c). Surprisingly, a large number of pits (around 18) with different coverage areas were observed in the L_{532} sample after the electrochemical exposure. However, in all pits, the LIPSS structures were present even after the material loss beneath these structures.

3.4. Tafel curves and corrosion rates

Fig. 9a shows the Tafel curves obtained by plotting logarithmic values of current density to the applied potential for all the samples. The corrosion potential of L_{Gv} and L_{1064} was more negative than the L_0 and L_{532}.

Fig. 9b shows the corrosion rates of all samples after extrapolating the Tafel curves. In general, all irradiated samples show better corrosion resistance than the L_0. The L_0 surface had the highest corrosion rate of 4.47 (±0.65) mm/year. The more corrosion-resistant surface was L_{532}, where the corrosion rate was 0.09 (± 0.04) mm/year. The ratio of increase in the corrosion resistance or decrease in the corrosion rate for all irradiated samples in comparison to the control sample (L_0) is presented in Fig. 9c. The L_{532} surface showed increased corrosion resistance nearly up to 50 folds to that of L_0.

The application of laser texturing on metallic surfaces has already shown the improved corrosion resistance to 7 folds [29] and 11 folds [33] as compared to the untreated samples. This improved corrosion behavior is due to the entrapment of air bubbles in the grooves, which can prevent the penetration of corrosive ions (e.g. Cl^-) to the patterned metallic surface [33]. These traps reduce the fractional area of the solid (LIPSS) – liquid (HBSS) interface, thus causing improved corrosion resistance. The same phenomenon is also reported in the studies [34,50,51] that decreased solid-liquid (electrode-electrolyte) contact area decreases the rate of corrosion.

Based on the aforementioned studies, the corrosion resistance or corrosion rate highly depends on the ratio of actual exposed surface area to the estimated exposed surface area. The actual exposed surface area is reduced due to the air bubbles entrapment between the LIPSS structures and in the grooves in all laser-induced periodic surface samples. Therefore, the penetration of corrosive ions of HBSS to the 316 L surface is prevented. Consequently, all laser-patterned samples showed better corrosion resistance. Moreover, the order of increasing corrosion resistance in laser patterned samples is $L_{1064} < L_{Gv} < L_{532}$ which is similar order to that of surface energies, suggesting the direct correlation between the surface energies and the corrosion resistance for irradiated samples.

3.5. Biocompatibility

All samples (both polished and LIPSS treated) demonstrate comparable level of cell attachment after plating (Fig. 10A) with no significant difference between the groups at day 1. UCMSCs exhibit good proliferation rate with appropriate metabolic activity, measured by the resazurin reduction assay, in days 2 and 3. L_{1064} surface demonstrate better proliferation of UCMSCs with the significant difference compare the L_{532}. Fluorescent DAPI staining (Fig. 10B) indicates complete cell confluence in both polished and LIPSS surfaces after 3 days of cultivation. Cell distribution on L_0 and L_{Gv} are more chaotic compared with the linear laser nanostructured surfaces, demonstrated by SEM images, while the cells become elongated and aligned along the LIPSS grooves in L_{1064} and L_{532} surfaces (Fig. 10C).

To provide measurable evidence, the assessment of Feret diameters, indexes and angles were done. Minimum Feret diameter was significantly decreased in all laser-treated samples with simultaneous decrease of the maximum Feret diameter in samples L_{1064} and L_{Gv} (Table 6 and Fig. 11). Significant decrease of Feret index of UCMSCs on samples L_{1064} and L_{532} suggests the influence of LIPSS pattern on cell shape and their elongation during the 3 days of proliferation. It is important to assess not only cell shape but their orientation along the LIPSS, taking into account the foreseen application of technology for the stent treatment. It was previously shown that the position of endothelial cells parallel to the flow of blood stream could decrease probability of plague formation and restenosis complications [52]. Our data clearly demonstrate that both L_{1064} and L_{532} nanopatterns provide appropriate cues for the alignment of the cells along the linear nanostructures. In addition, the L_{Gv} surface demonstrates wider peak of a larger distribution of cell angle due to the crosshatch structure of this surface.

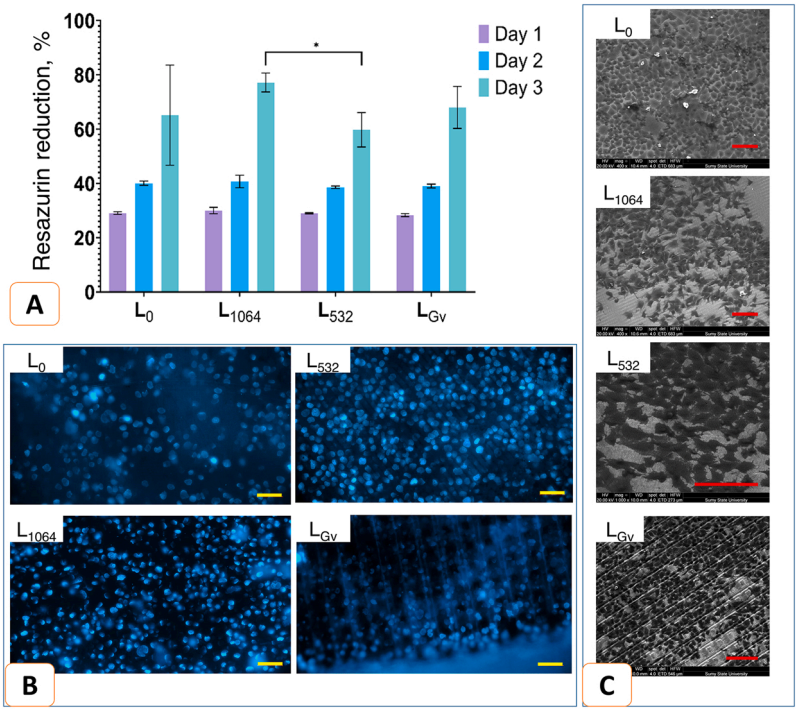

Fig. 10. Resazurin reduction assay representing the dynamic of UCMSC proliferation (A), with fluorescent DAPI staining (B) and SME images (C) in day 3 after plating. * Designates statistical significance at $p \leq 0.05$ (unpaired Welch's *t*-test). Scale bars are 50 μm (B) and 100 μm (C).

Table 6
Resulted table of Feret diameter, angle and index for UCMSC cells in day 3 of proliferation on the treated and non-treated (polished) surfaces.

Sample	Maximum Feret diameter	Minimum Feret diameter	Feret index	Feret Angle	LIPSS angle on sample
L_0	29.01±9.350	18.95±6.000	0.6685±0.1436	83.64±50.09	-
L_{1064}	24.30±6.338	13.46±3.717	0.5636±0.1220*	93.62±48.27	127.7±9.279
L_{532}	29.35±8.207	13.57±3.185	0.4939±0.1628***	129.0±52.05	159.9±1.545
L_{Gv}	22.99±6.420	13.90±4.382	0.6199±0.1473	72.60±50.01	32.67±0.1816

Note: Asterisks in the table signify statistical difference of L_{1064} and L_{532} in comparison to the control sample L_0 (*P<0.05; ***P<0.001).

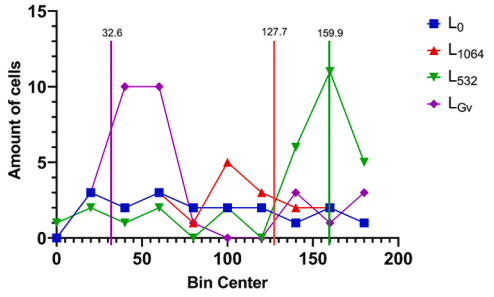

Fig. 11. Histogram of distribution of the angles between the relative position of the elongated cells and the of the LIPSS patterns. Vertical lines correspond to the angles between the axis on the coordinate system and the direction of the LIPSS pattern on the samples. Please note that the angle position of sample L_{Gv} (32.6°) closely coincides with the peak of distribution of cell angles of the corresponding sample (40–60°); the angle position of sample L_{1064} (128°) loosely coincides with the peak of distribution of cell angles of the corresponding sample (100°); and the angle position of sample L_{532} matches with the peak of distribution of cell angles of the corresponding sample (160°). The cell angle distribution of the control sample (L_0) does not show any peak which implies random positions of cells.

4. Conclusions

In this work, the biocompatibility, surface topography, surface free energy, and corrosion behavior of three different LIPSS structures on stainless steel 316 L were investigated in comparison with the untreated polished surfaces. All LIPSS samples showed increased roughness as compared to the polished sample. While the polished steel was hydrophilic, the LIPSS treated surface became hydrophobic. The shift from hydrophilicity to hydrophobicity was associated with the increased corrosion resistance of the nanostructured surfaces. We assume that the decreased rate of corrosion was due to a decreased solid-liquid (electrode-electrolyte) contact area. This was probably because the air bubbles trapped into the cavities that prevent the penetration of corrosive ions. The linear LIPSS structures behaved like coating and did not detach from the surface even after pit formation. Among all LIPSS samples, the L_{532} specimen showed excellent corrosion resistance complemented by significantly higher surface energy and the lowest corrosion rate. Meanwhile, the L_{1064} specimen showed the highest cell attachment and proliferation.

In general, LIPSS samples have a higher corrosion resistance due to the higher surface roughness, lesser solid-liquid contact area, more hydrophobic surfaces and higher surface energy. Moreover, LIPSSs provide an appropriate environment for cell attachment and proliferation with significant influence on cell shape and directional growth along the nano-grooves. Overall, the LIPSS patterns can be used on stent surfaces

in order to improve corrosion resistance, endothelialization, cell proliferation, platelet adhesion and cell alignment, leading to reduced rate of post surgery complications.

Declaration of Competing Interest

The authors declare that they have no known competing financial interests or personal relationships that could have appeared to influence the work reported in this paper.

Data availability

Data will be made available on request.

Acknowledgments

This work was supported by The European Virtual Institute on Knowledge-based Multifunctional Materials AISBL (KMM-VIN) in the frame of KMM-VIN Research Fellowship program [12th Call, 2020/21]. Cell culture study was supported under the MSCA-RISE project NanoSurf-777926. We thank Dr. Sukhvinder Sandhu for revising language in some parts of the manuscript.

References

[1] T. Doenst, A. Haverich, P. Serruys, et al., PCI and CABG for treating stable coronary artery disease: JACC review topic of the week, J. Am. Coll. Cardiol. 73 (2019) 964–976, https://doi.org/10.1016/J.JACC.2018.11.053.
[2] D.L. Brown, R.F. Redberg, Last nail in the coffin for PCI in a stable angina? Lancet 391 (2018) 3–4, https://doi.org/10.1016/S0140-6736(17)32757-5.
[3] R.K. Al-Lamee, A.N. Nowbar, D.P. Francis, Percutaneous coronary intervention for stable coronary artery disease, Heart 105 (2019) 11–19, https://doi.org/10.1136/HEARTJNL-2017-312755.
[4] U. Sigwart, J. Puel, V. Mirkovitch, et al., Intravascular stents to prevent occlusion and restenosis after transluminal angioplasty, N. Engl. J. Med. 316 (1987) 701–706, https://doi.org/10.1056/NEJM198703193161201.
[5] D.R. Holmes, M. Savage, J.M. LaBlanche, et al., Results of Prevention of REStenosis with Tranilast and its Outcomes (PRESTO) trial, Circulation 106 (2002) 1243–1250, https://doi.org/10.1161/01.CIR.0000028335.31300.DA.
[6] Serruys P.W., Strauss B.H., Beatt K.J., et al. (1991) Angiographic Follow-up after Placement of a Self-Expanding Coronary-Artery Stent. 324:13–17. doi:10.1056/NEJM199101033240103.
[7] R. Rossini, G. Musumeci, A. Aprile, O. Valsecchi, Long-term outcomes in patients undergoing percutaneous coronary intervention with drug-eluting stents, Expert Rev. Pharmacoecon. Outcomes Res. 10 (2010) 49–61, https://doi.org/10.1586/ERP.10.1.
[8] O.F. Bertrand, R. Sipehia, R. Mongrain, et al., Biocompatibility aspects of new stent technology, J. Am. Coll. Cardiol. 32 (1998) 562–571, https://doi.org/10.1016/S0735-1097(98)00289-7.
[9] M. SO, M. AR, Bench to bedside: the development of rapamycin and its application to stent restenosis, Circulation 104 (2001) 24–25, https://doi.org/10.1161/01.CIR.104.8.852.
[10] I.B.A. Menown, R. Noad, E.J. Garcia, I. Meredith, The platinum chromium element stent platform: from alloy, to design, to clinical practice, Adv. Ther. 27 (2010) 129–141, https://doi.org/10.1007/S12325-010-0022-9.
[11] A. Colombo, J. Drzewiecki, A. Banning, et al., Randomized study to assess the effectiveness of slow- and moderate-release polymer-based paclitaxel-eluting stents for coronary artery lesions, Circulation 108 (2003) 788–794, https://doi.org/10.1161/01.CIR.0000086926.62288.A6.
[12] G. El-Hayek, F. Messerli, S. Bangalore, et al., Meta-analysis of randomized clinical trials comparing short-term versus long-term dual antiplatelet therapy following drug-eluting stents, Am. J. Cardiol. 114 (2014) 236–242, https://doi.org/10.1016/J.AMJCARD.2014.04.035.
[13] L. Holmvang, H. Kelbæk, A. Kaltoft, et al., Long-term outcome after drug-eluting versus bare-metal stent implantation in patients with ST-segment elevation myocardial infarction: 5 years follow-up from the randomized DEDICATION trial (Drug Elution and Distal Protection in Acute Myocardial Infarction), JACC Cardiovasc. Interv. 6 (2013) 548–553, https://doi.org/10.1016/J.JCIN.2012.12.129.
[14] A. Shahryari, F. Azari, H. Vali, S. Omanovic, The response of fibrinogen, platelets, endothelial and smooth muscle cells to an electrochemically modified SS316LS surface: towards the enhanced biocompatibility of coronary stents, Acta Biomater. 6 (2010) 695–701, https://doi.org/10.1016/J.ACTBIO.2009.07.007.
[15] Z. Yang, J. Wang, R. Luo, et al., The covalent immobilization of heparin to pulsed-plasma polymeric allylamine films on 316L stainless steel and the resulting effects on hemocompatibility, Biomaterials 31 (2010) 2072–2083, https://doi.org/10.1016/J.BIOMATERIALS.2009.11.091.
[16] M. Saqib, O. Kuzmin, H. Kraskiewicz, et al., Evaluation of in vitro corrosion behavior of titanium oxynitride coated stainless steel stents, IEEE Access 9 (2021) 59766–59782, https://doi.org/10.1109/access.2021.3072597.
[17] N. Beshchasna, A.Y.K. Ho, M. Saqib, et al., Surface evaluation of titanium oxynitride coatings used for developing layered cardiovascular stents, Mater. Sci. Eng. C 99 (2019) 405–416, https://doi.org/10.1016/j.msec.2019.01.131.
[18] K. Zhang, T. Liu, J.A. Li, et al., Surface modification of implanted cardiovascular metal stents: from antithrombosis and antirestenosis to endothelialization, J. Biomed. Mater. Res. 102 (2014) 588–609.
[19] J. Dong, M. Pacella, Y. Liu, L. Zhao, Surface engineering and the application of laser-based processes to stents—a review of the latest development, Bioact. Mater. 10 (2022) 159–184, https://doi.org/10.1016/J.BIOACTMAT.2021.08.023.
[20] J. Bonse, Quo vadis LIPSS?—recent and future trends on laser-induced periodic surface structures, Nanomaterials 10 (2020) 1–19, https://doi.org/10.3390/nano10101950.
[21] Y. Kotsiuba, I. Hevko, S. Bellucci, I. Gnilitskyi, Bitmap and vectorial hologram recording by using femtosecond laser pulses, Sci. Rep. 111 (11) (2021) 1–8, https://doi.org/10.1038/s41598-021-95665-5, 2021.
[22] L. Orazi, I. Gnilitskyi, I. Pavlov, et al., Nonlinear laser lithography to control surface properties of stainless steel, CIRP Ann. 64 (2015) 193–196, https://doi.org/10.1016/J.CIRP.2015.04.038.
[23] C. Kunz, J. Bonse, D. Spaltmann, et al., Tribological performance of metal-reinforced ceramic composites selectively structured with femtosecond laser-induced periodic surface structures, Appl. Surf. Sci. 499 (2020), 143917, https://doi.org/10.1016/J.APSUSC.2019.143917.
[24] I. Gnilitskyi, A. Rota, E. Gualtieri, et al., Tribological properties of high-speed uniform femtosecond laser patterning on stainless steel, Lubricants 7 (2019), 83, https://doi.org/10.3390/LUBRICANTS7100083.
[25] I. Gnilitskyi, M. Pogorielov, R. Viter, et al., Cell and tissue response to nanotextured Ti6Al4V and Zr implants using high-speed femtosecond laser-induced periodic surface structures, Nanomedicine 21 (2019), 102036, https://doi.org/10.1016/J.NANO.2019.102036.
[26] S. Gräf, Formation of laser-induced periodic surface structures on different materials: fundamentals, properties and applications, Adv. Opt. Technol. 9 (2020) 11–39, https://doi.org/10.1515/aot-2019-0062.
[27] E. Stratakis, J. Bonse, J. Heitz, et al., Laser engineering of biomimetic surfaces, Mater. Sci. Eng. R Rep. 141 (2020), 100562, https://doi.org/10.1016/j.mser.2020.100562.
[28] M.T. Mohammed, Z.A. Khan, A.N. Siddiquee, Surface modifications of titanium materials for developing corrosion behavior in human body environment: a review, Procedia Mater. Sci. 6 (2014) 1610–1618, https://doi.org/10.1016/j.mspro.2014.07.144.
[29] Yue T.M., Yu J.K., Mei Z., Man H.C. (2002) Excimer laser surface treatment of Ti-6Al-4V alloy for corrosion resistance enhancement.
[30] R. Singh, S.K. Tiwari, S.K. Mishra, N.B. Dahotre, Electrochemical and mechanical behavior of laser processed Ti-6Al-4V surface in Ringer's physiological solution, J. Mater. Sci. Mater. Med. 22 (2011) 1787–1796, https://doi.org/10.1007/s10856-011-4362-z.
[31] M. Geetha, U.K. Mudali, N.D. Pandey, et al., Microstructural and corrosion evaluation of laser surface nitrided Ti-13Nb-13Zr alloy, Surf. Eng. 20 (2004) 68–74, https://doi.org/10.1179/026708404225010595.
[32] Y. Jang, W.T. Choi, C.T. Johnson, et al., Inhibition of bacterial adhesion on nanotextured stainless steel 316L by electrochemical etching, ACS Biomater. Sci. Eng. 4 (2018) 90–97, https://doi.org/10.1021/acsbiomaterials.7b00544.
[33] L.R. de Lara, R. Jagdheesh, J.L. Ocaña, Corrosion resistance of laser patterned ultrahydrophobic aluminium surface, Mater. Lett. 184 (2016) 100–103, https://doi.org/10.1016/j.matlet.2016.08.022.
[34] R. Ramachandran, M. Nosonovsky, Coupling of surface energy with electric potential makes superhydrophobic surfaces corrosion-resistant, Phys. Chem. Chem. Phys. 17 (2015) 24988–24997, https://doi.org/10.1039/C5CP04462F.
[35] H. Qiu, P. Qi, J. Liu, et al., Biomimetic engineering endothelium-like coating on cardiovascular stent through heparin and nitric oxide-generating compound synergistic modification strategy, Biomaterials 207 (2019) 10–22, https://doi.org/10.1016/j.biomaterials.2019.03.033.
[36] Barrere F., Van Blitterswijk C.A., De Groot K., Layrolle P. (2002) Nucleation of biomimetic Ca-P coatings on Ti6Al4V from a SBF Â 5 solution: influence of magnesium.
[37] W. Cui, E. Beniash, E. Gawalt, et al., Biomimetic coating of magnesium alloy for enhanced corrosion resistance and calcium phosphate deposition, Acta Biomater. 9 (2013) 8650–8659, https://doi.org/10.1016/j.actbio.2013.06.031.
[38] M. Martínez-Calderon, R.J. Martín-Palma, A. Rodríguez, et al., Biomimetic hierarchical micro/nano texturing of TiAlV alloys by femtosecond laser processing for the control of cell adhesion and migration, Phys. Rev. Mater. 4 (2020), 056008, https://doi.org/10.1103/PHYSREVMATERIALS.4.056008/FIGURES/7/MEDIUM.
[39] C. Liang, Y. Hu, H. Wang, et al., Biomimetic cardiovascular stents for in vivo re-endothelialization, Biomaterials 103 (2016) 170–182, https://doi.org/10.1016/j.biomaterials.2016.06.042.
[40] J. Bonse, S. Gräf, Ten open questions about laser-induced periodic surface structures, Nanomaterials 11 (2021), 3326, https://doi.org/10.3390/nano11123326.
[41] N. Selvakumar, H.C. Barshilia, K.S. Rajam, Effect of substrate roughness on the apparent surface free energy of sputter deposited superhydrophobic polytetrafluoroethylene coatings: a comparison of experimental data with different theoretical models, J. Appl. Phys. 108 (2010), 013505, https://doi.org/10.1063/1.3456165.

[42] A. Kozbial, Z. Li, C. Conaway, et al., Study on the surface energy of graphene by contact angle measurements, Langmuir 30 (2014) 8598–8606, https://doi.org/10.1021/la5018328.
[43] K. Song, J. Lee, S.O. Choi, J. Kim, Interaction of surface energy components between solid and liquid on wettability, and its application to textile anti-wetting finish, Polymers 11 (2019), 498, https://doi.org/10.3390/POLYM11030498.
[44] Z. Zhang, W. Wang, A.N. Korpacz, et al., Binary liquid mixture contact-angle measurements for precise estimation of surface free energy, Langmuir 35 (2019) 12317–12325, https://doi.org/10.1021/acs.langmuir.9b01252.
[45] M.A.F. Martinez, F. Balderrama Í de, P.S.B.H. Karam, et al., Surface roughness of titanium disks influences the adhesion, proliferation and differentiation of osteogenic properties derived from human, Int. J. Implant Dent. 6 (2020), 46, https://doi.org/10.1186/s40729-020-00243-5.
[46] G. Chinga, O. Gregersen, B. Dougherty, Paper surface characterisation by laser profilometry and image analysis, Microsc. Anal. 96 (2003) 21–23.
[47] S. Kyrylenko, F. Warchoł, O. Oleshko, et al., Effects of the sources of calcium and phosphorus on the structural and functional properties of ceramic coatings on titanium dental implants produced by plasma electrolytic oxidation, Mater. Sci. Eng. C 119 (2021), 111607, https://doi.org/10.1016/j.msec.2020.111607.
[48] M. Palencia, Surface free energy of solids by contact angle measurements, J. Sci. Technol. Appl. 2 (2017) 84–93, https://doi.org/10.34294/j.jsta.17.2.17.
[49] Y. Sun, C.J. Radke, B.D. McCloskey, J.M. Prausnitz, Wetting behavior of four polar organic solvents containing one of three lithium salts on a lithium-ion-battery separator, J. Colloid Interface Sci. 529 (2018) 582–587, https://doi.org/10.1016/j.jcis.2018.06.044.
[50] D. Lv, J. Ou, M. Xue, F. Wang, Stability and corrosion resistance of superhydrophobic surface on oxidized aluminum in NaCl aqueous solution, Appl. Surf. Sci. 333 (2015) 163–169, https://doi.org/10.1016/J.APSUSC.2015.02.012.
[51] N. Wang, D. Xiong, Superhydrophobic membranes on metal substrate and their corrosion protection in different corrosive media, Appl. Surf. Sci. 305 (2014) 603–608, https://doi.org/10.1016/j.apsusc.2014.03.142.
[52] Z. Wang, N.K. Putra, H. Anzai, M. Ohta, Endothelial cell distribution after flow exposure with two stent struts placed in different angles, Front. Physiol. 12 (2022), https://doi.org/10.3389/FPHYS.2021.733547.